International Journal of Hydrogen Energy 252 (2026) 156079

Contents lists available at ScienceDirect

International Journal of Hydrogen Energy

journal homepage: www.elsevier.com/locate/he

Deformation bands as flow barriers in an underground hydrogen storage system

Douglas Smith [a,c,*], Edward Hough [a], Daniel Arnold [b], Oliver Wakefield [a], Zaid Jangda [c], Kamaljit Singh [b], Andreas Busch [c]

[a] British Geological Survey, Keyworth, NG12 5GG, United Kingdom
[b] Institute for GeoEnergy Engineering, Heriot-Watt University, Edinburgh, EH14 4AS, United Kingdom
[c] Lyell Centre, Heriot-Watt University, Edinburgh, EH14 4AS, United Kingdom

ABSTRACT

To enable hydrogen (H_2) to substantially contribute to the energy transition, a better understanding of the efficacy of large-scale underground hydrogen storage (UHS) is needed. Storage options in porous rocks such as reservoirs and saline aquifers offer the largest potential by volume. However, sandstone reservoirs are typically characterised by different degrees of heterogeneity that affect storage. Heterogeneities include deformation bands, often found in well-sorted aeolian sandstone with good UHS potential. Deformation bands are planar, low-permeability features that can develop through grainsize reduction and fusing in response to changes in stress. Little is known about the effect of heterogeneities on the injection, storage and recovery of H_2. Therefore, this study examines the effect of permeability contrasts caused by deformation bands on UHS. To do this we undertake two cycles of H_2 injection and production in a two-phase (H_2-brine) flow experiment on a Sherwood Sandstone sample containing a deformation band at 50 °C and 10 MPa in an X-ray micro Computed Tomography scanner. In addition, we repeat the experiment with helium to further evaluate effects of the permeability contrasts and understand whether helium can be a useful proxy for H_2 in laboratory-based experiments. The results show that the deformation band analysed is a baffle to flow, increasing the required injection pressure for gas transit, and there are few pathways for H_2 across it. In the first cycle very little H_2 is trapped below and in the deformation band. But when the pathways become blocked during imbibition, due to brine snap off, there is a substantial increase in H_2 trapping, reducing H_2 flow and production. We also see trapping of H_2 in larger pores and post injection movement of H_2. Both processes exhibit similar characteristics, with H_2 occupying the pore centres and brine on the rock surfaces. Our observations will assist in understanding processes within UHS reservoirs and enable strategies to be developed to deal with fluid movement and pressure changes resulting from permeability contrasts. There are many similarities in the behaviour of H_2 and helium in our experiment, confirming our observations with H_2. As such, we find that helium can be used as a proxy in these conditions, although adjustments may need to be made for the viscosity differences.

1. Introduction

Hydrogen (H_2) allows for increased use of alternative energy sources and reduction of our dependence on hydrocarbons [1]. It can be utilised to store energy in times of oversupply and used when energy demand is high and for hard to decarbonise processes [2]. Meeting demand, particularly seasonal requirements, necessitates large quantities of H_2 storage. Globally, by 2035, it is predicted that 230 TWh is needed to be on course to attain Net Zero by 2050 [3,4]. Underground hydrogen storage (UHS) is necessary to meet this target [4].

H_2 storage in salt caverns is close to reaching market readiness but is not geographically available to all. Further research is needed into the effect of frequent injection and production cycles ("fast cycling") and repurposing existing salt caverns [4–6]. UHS in porous media, either aquifers or depleted hydrocarbon reservoirs, offers considerably larger storage capacities in reservoirs that are geographically more widespread [5]. However, questions remain related to the efficiency of H_2 storage in porous rocks, which is highly dependent on reservoir quality and character.

Currently there is high uncertainty in the effectiveness of the production process, including the recovery efficiency and purity of produced H_2 [6]. Recovery efficiency describes the proportion of injected H_2 that can be produced, known as the 'recovery factor' [7], calculated by:

$$\textit{Recovery factor} = \frac{S_{gi} - S_{gr}}{S_{gi}} \quad \text{Eq 1}$$

where S_{gi} is the initial gas saturation (pre-production) and S_{gr} is the residual gas saturation (post-production).

The efficacy of UHS and the storage capacity of a reservoir are dependent on heterogeneities in the rock, created by sedimentary or

* Corresponding author. British Geological Survey, Keyworth, NG12 5GG, United Kingdom
E-mail address: dosmi@bgs.ac.uk (D. Smith).

https://doi.org/10.1016/j.ijhydene.2026.156079
Received 1 February 2026; Received in revised form 25 May 2026; Accepted 13 June 2026
Available online 24 June 2026

structural processes [8]. The former determines properties of the host rock, such as porosity and permeability, as a result of the depositional environment, subsequent diagenesis and sedimentary architecture. In relation to siliclastic rocks, the sedimentary processes result in a range of sandstones from those with high lateral continuity, to complex interlocking, jigsaw bedding [9,10]. Structural features, such as faulting, can affect the reservoir by providing boundaries or flow pathways but, as with sedimentary processes, there are more localised features that affect fluid movement on a smaller scale. Deformation bands are typically smaller scale planar structural heterogeneities that are acknowledged barriers to fluid flow [11]. We study the influence of deformation bands on rock-fluid interactions to understand implications for reservoir-scale processes.

Despite the recent attention UHS has received, particularly since 2018, research gaps have been identified [12]. These include the effect of reservoir heterogeneity on injection, storage and production of H_2 as there is limited experimental data for heterogeneous reservoir rocks. This may be particularly important due to the cyclical nature of UHS, as negative impacts, such as the trapping or diffusion and dispersion of H_2, might be aggregated. Numerical modelling research that specifically examines the effect of heterogeneity finds that it has a significant effect on reservoir performance with respect to migration patterns, gas mixing, hysteresis and structural trapping, including compartmentalisation [8,13–16]. These processes impact the efficacy of UHS by affecting the recovery factor, purity of produced gas and reservoir capacity.

Of the few H_2-based fluid flow studies that observe behaviour in heterogeneous samples, Boon and Hajibeygi [17] investigate fluid flow in a sample of Berea sandstone with two low porosity bands. The authors measure H_2 and brine relative permeabilities and image the movement of H_2. However, although they note that the bands act as a capillary barrier, dispersing the flow of H_2, they do not focus on the effects of the permeability contrasts. Jangda et al. [18] used a layered sample and found that the permeability contrast between layers reduced the pathways through the low permeability layer, trapping H_2 during imbibition. We build on this research and concentrate on the larger permeability contrasts observed between deformation bands and host rock. Here, reduced pore and throat sizes intensify rock-fluid interactions, amplifying the role of capillary forces, the relative attraction of different fluids to the rock, and hence the fluid distribution. Consequently, we study the effect of permeability contrasts on UHS by examining two-phase fluid flow in a sandstone sample containing a deformation band from the UK Sherwood sandstone, representative of rock being considered for large-scale H_2 storage. In addition, we verify the results from the H_2 experiment by using helium as an analogue gas.

2. Materials and experimental reasoning

2.1. Sherwood Sandstone

We experimentally analyse two-phase flow within the Triassic Sherwood Sandstone. The Sherwood Sandstone is a prolific hydrocarbon reservoir, and together with the underlying Permian sandstone, it is the UK's second largest aquifer [19–21]. In addition to potential H_2 storage, the formation has other competing future applications, such as storage for carbon dioxide, compressed air and thermal energy as well as a source of geothermal energy [21,22].

The Permo-Triassic sandstones were deposited in a mixed fluvial and aeolian environment, resulting in a succession with a variety of facies associations [22]. In the East Irish Sea and Cheshire Basins, towards the west of the UK, the highest porosities and permeabilities tend to be found within aeolian and dune facies, due to the rounded and well-sorted nature of the grains. This results in porosities up to 30% and permeabilities $>10^{-11}$ m^2 (10 D) [22–24]. Therefore, the aeolian and dune units, on the face of it, provide reservoirs with the most beneficial storage properties and have a disproportionate effect, compared to other facies, on hydrocarbon production [23]. However, aeolian facies and those with a reduced content of silt and clay-grade grainsizes may be more prone to the development of deformation bands that can reduce flow locally [22].

The Sherwood Sandstone sample used in this study was obtained from the Saughall Massie borehole, Cheshire (BGS [25], reference number SJ28NW/22). This borehole proves the upper part of the Sherwood Sandstone, comprising the Helsby Sandstone Formation. The upper part of the Helsby Sandstone is termed the Frodsham Member, which is predominantly aeolian and lies between 137.83 and 117.28 m depth. Visually, the sample is a red-brown sandstone with rounded, mostly medium-sized grains, indicative of an aeolian dune facies. There is little evidence of bedding, but the core contains deformation bands.

2.2. Deformation bands

Deformation bands are planar features developed within the sandstone created by the localisation of stress and strain. The forces the rock experiences are sufficient to crush individual grains and alter the rock structure, typically with up to a centimetre displacement across the band [26]. The structure of the rock can be altered either by the movement of the grains, creating disaggregation or phyllosilicate bands, or by the breaking and re-fusing of grains. We are concerned with the latter, termed cataclastic deformation bands, as these often have the largest effect on reservoir properties [26]. Due to the cataclasis of grains, particularly of feldspar, and subsequent diagenetic cementation, the bands often have reduced porosity and permeability [11,22]. However, as deformation bands vary in thickness and composition along their length, porosity and permeability also varies [26]. Porosity has been measured to be reduced from about 30% to 10% or less in coarser grained sandstone, and permeability was found to be several orders of magnitude lower than the host rock [11,27]. Even though individual bands may only be millimetres to centimetres thick they have planar faces that are often broadly aligned with localised faulting, although the dip is often sub-parallel to the fault [26]. Bands can extend up to hundreds of metres, particularly when they exist as part of clusters or conjugate arrangements (Fig. 1) [22,26]; conjugate bands also have a second slip face oriented in an opposing direction (seen in cross-section in Fig. 1a) [26].

As a result of the altered porosity and permeability, bands can present a barrier to fluid flow, alter fluid pathways and potentially compartmentalise the reservoir [11,28]. The planar faces of the deformation bands direct flow parallel to the bands [29]. Therefore, even though the bands create relatively small heterogeneity within a reservoir, they can affect plume development, create localised, anomalous pressure gradients and reduce the reservoir capacity [8,30]. There is some uncertainty about the impact deformation bands may have as the porosity and permeability variations are non-uniform [29,31].

Deformation bands are significantly more abundant in well-sorted, aeolian sandstone compared to other depositional settings [22,28]. While such sandstones show great potential for UHS, deformation bands have the potential to significantly affect reservoir behaviour, especially at lower pressures. Furthermore, deformation bands are often below seismic and sometimes even below wireline logging resolution [11,32]. Therefore, we need to ascertain their impact on fluid flow and reservoir performance to develop a checklist of influential UHS reservoir characteristics.

As stated, two studies report on the effect of permeability contrasts in sandstone and implications for H_2-water fluid flow experiments. Both studies address permeability contrasts of 1-2 orders of magnitude, not as large as expected from many deformation bands. Jangda et al. [18] observed flow in a vertical plane, whereas Boon and Hajibeygi [17] experimented with flow in the horizontal plane. This enabled Boon and Hajibeygi [17] to observe the gravity segregation of the fluids due to the density difference. However, they found that the low porosity band enhanced the mixing of the two fluids. Unfortunately, the resolution in the latter study was not sufficient to determine the pathways that led to

Fig. 1. a) Conjugate (diamond-shaped) deformation bands in a vertical cutting at Grange Hill, Wirral, NW England and b) a cluster of braided deformation bands on a horizontal surface of an outcrop at Thurstaston Common, Wirral, NW England. 30 cm ruler in each image for scale.

the mixing. Romano et al. [33] undertook a two-phase flow (CO_2-water) experiment on a deformation band from the Navajo sandstone (Utah, USA). They found that deformation bands contribute to compartmentalisation of the reservoir, increasing structural trapping. We observe the effect of a deformation band on fluid (H_2 and brine) flow pathways at the pore scale over two cycles of drainage and imbibition to understand implications for UHS.

2.3. *Using helium as a proxy for H_2*

Other gases have been used as a substitute for H_2 in experiments and modelling. This was motivated by both the extensive literature with respect to gases like CO_2 and CH_4, and because of safety concerns posed when experimenting with H_2 in confined laboratory environments [34]. The existing literature predominantly relates to trapping, such as for CO_2 storage, or natural gas storage and production [35,36]. Such research rarely relates to the cyclic nature of injection and production that are fundamental to UHS, where any hysteresis within the system will have an impact.

There are mixed results for proxies for H_2. Contact angles for H_2, CH_4 and N_2 and their interfacial tension with water have shown to be similar [34,37]. Drainage relative permeabilities of H_2, CH_4 and N_2 have been measured in two studies. Higgs et al. [34] found relative permeabilities to be similar in shallow reservoir settings. In their investigation they adjusted injection flow rates to compensate for the viscosity differences. Manoorkar et al. [38] maintained similar flow rates for the 3 gases and found that only the relative permeabilities of H_2 and CH_4, and not N_2, were alike. Furthermore, other studies have found that N_2 is an unreliable proxy, as it does not behave in the same way as H_2, particularly in relation to gas-trapping during imbibition, storage capacity and post-injection redistribution [37,39]. Using CH_4 data also presents a problem as it changes from gaseous to supercritical phase at reservoir conditions above 4.6 MPa. Finally, Bo et al. [40] used CO_2-brine relative permeability relationships as a substitute for UHS reservoir modelling and found that the outcomes substantially diverged from using a measured H_2-brine relationship.

In two studies, helium is used to develop an injection protocol for H_2 and as a proxy for H_2 diffusion in halite [41] [42]. In both instances there is an assumption that the two gases behave similarly, which may be reasonable based upon their molecular masses and interfacial tensions with brine (both about 68 mN m^{-1} at reservoir conditions of 10 MPa and 50 °C) [43]. However, there is a difference in density (7.2 kg m^{-3} for H_2 versus 14.4 kg m^{-3} for helium) [44]. Our study tests the assumption that the gases are similar under reservoir conditions. Additionally, the helium-brine experiment provides supplementary evidence to understand how two-phase, gas-brine flow interacts with the deformation band. For instance, it may confirm whether the deformation band acts as a barrier to flow and if there are pathways across it.

3. Methods

3.1. *Sample characteristics and properties*

3.1.1. *Bulk mineralogy*

Bulk mineralogy was carried out by James Hutton Ltd Analytical Laboratory Services (Aberdeen, UK) on a trim end from the sample shown in Fig. 2, which did not contain a deformation band. The results are summarised in Table 1. The sample is dominated by quartz (82.4%) and feldspar (10.3%) with minor amounts of hematite, siderite and clay. The latter is predominantly illite and illite/smectite mixed layers (5.8%).

The quartz content is higher than in sandstones from legacy wells in the Southern North Sea (maximum 64.4% quartz) studied by Rushton et al. [45] and closer to the samples used in other two-phase flow experiments (81% - 95% quartz) [17,46,47].

3.1.2. *Porosity and permeability*

Porosity measurements have been conducted via scanning electron microscopy (SEM) images of a thin section taken from the same deformation band, adjacent to the sample. This resulted in 27.5% and 29.0% in the intact rock either side of the deformation band, and 9.9% in the deformation band. Porosity was further determined from X-ray micro Computed Tomography (μCT) images, yielding comparable values of 25.2% and 24.9% in the intact rock and 12.6% in the deformation band.

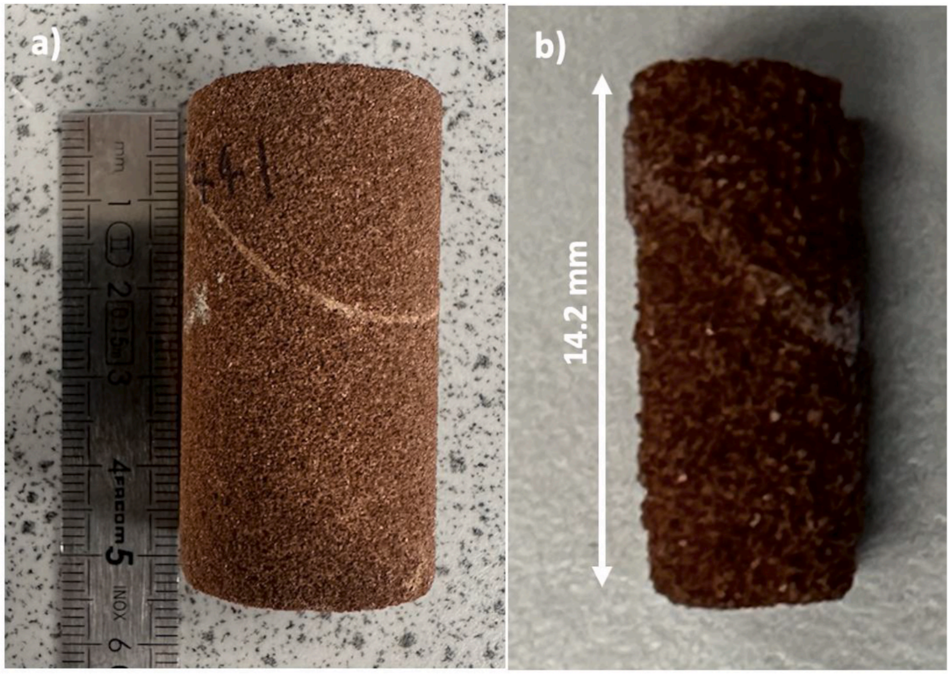

Fig. 2. a) 1″ diameter core sample taken from the Frodsham member of the Helsby Sandstone Formation containing a deformation band. b) 6 mm diameter sub-sample cut from a) with the same deformation band running across it.

Table 1
Results from the bulk mineralogy (in wt-%). Testing performed on a sample from the Frodsham member of the Helsby Sandstone Formation. I + I/S ML represents illite and illite/smectite mixed layers.

Quartz	Plagioclase	K-feldspar	Siderite	Hematite	Kaolinite	Chlorite	Mica	I + I/S-ML	Total
82.4	0.5	9.8	0.1	0.9	0.1	0.2	0.2	5.8	100.0

In addition, we undertook a generalised network extraction using the PoreXtractor software [48,49]. The software first extracts pore and pore throat data from the dry µCT scan, using an algorithm to identify the largest voids (pores). Then spheres are fitted into pores and pore throats. Once the pores and throats within the network have been classified, a network model is created, enabling the calculation of pore and throat radii and distributions [50]. The network model is superimposed onto the fluid image data, identifying the fluid predominantly occupying each pore and throat after each injection, allowing fluid saturations to be assessed. We apply this process to each of the sample sections (top, deformation band and bottom, Fig. 5) and the pore and throat distributions are displayed in Fig. 3. The pore and throat distribution in the intact core above and below the deformation band are similar, whereas the deformation band has a higher proportion of smaller pores and pore throats. It should be noted that the resolution of the images was 5 µm per voxel, so frequencies of smaller pore and throat radii should be treated with caution and pores and throats with radii of less than 2-3 voxels would not be resolved.

Permeability was measured using a nitrogen permeameter at Heriot-Watt University and the measurements were calibrated to correct for gas slippage [51]. The intact core (excluding deformation bands) shows permeabilities exceeding 10^{-12} m^2 (1 Darcy) in both horizontal and vertical orientations. These values are consistent with measurements reported by Bloomfield et al. [24] who measured permeabilities in aeolian sandstone ranging from 4.0 x 10^{-13} m^2 (410 mD) to 2.7 x 10^{-12} m^2 (2.7 D). The samples containing a deformation band show average permeabilities (across the whole sample of intact rock and deformation band) between ~100 and 300 mD. Deformation band permeabilities between 4.4 x 10^{-15} m^2 (4.4 mD) and 8.3 x 10^{-15} m^2 (8.4 mD) are calculated from these average permeability measurements. For these calculations it is assumed that the deformation band is oriented perpendicular to fluid flow and has uniform permeability.

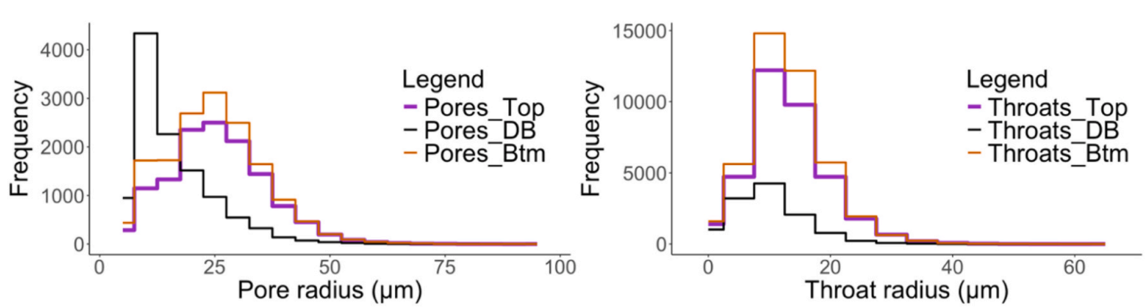

Fig. 3. Pore (left) and throat (right) distribution in the deformation band and the intact rock above and below the deformation band.

3.2. Rock and fluids

We used the experimental methods detailed in Jangda et al. [18] as a foundation to test the effect of the deformation band on both H_2-brine and helium-brine flow. We therefore only provide a summary of the setup here.

Initially, 1" (2.54 cm) diameter samples were extracted from drill core (between the depths of 124 m and 133.5 m). These were used to test the horizontal and vertical permeability of the sandstone and the reduction in permeability caused by the deformation band (see above). Subsequently, a mini core (6 mm diameter, 14.2 mm long) was plugged from a depth of 135 m (Fig. 2) for further testing.

The sample was cleaned in methanol and oven dried at 105 °C for 12 h. It was then wrapped in Teflon tape and aluminium foil, keeping the rock ends uncovered, and placed in a Viton sleeve. Next, this assemblage was placed in a core holder so that the deformation band was closer to the top of the sample, allowing fluid movement below the deformation band to be observed.

Brine, de-ionised water and potassium iodide (4 wt-%), was prepared gravimetrically using a magnetic stirrer at room temperature. The composition of the brine was chosen to improve the contrast between the fluids in the X-ray μCT images. Prior to injection, brine was equilibrated with H_2 and helium (BOC, 99.999% purity) at 50 °C and 10 MPa using a Hastelloy reactor (Parr Instruments Company, USA) to prevent injected gas being dissolved (for details, see Ref. [47]).

3.3. Experimental apparatus

The experimental apparatus configuration is shown in Fig. 4. The core holder was placed vertically on a rotating stage within the X-ray μCT scanner (EasyTom 150, RX Solutions, FR). A vertical section (6.4 mm) of the sample was scanned. All scans were acquired with a voxel size of 5 μm, with 1792 projections. The tube voltage was 90 kV and X-ray tube power was 10 W. The scanning time was just under 1h 50 min.

For the drainage cycles, we injected H_2 or helium from the top of the sample. Brine was injected from the base of the sample (imbibition). The flow system allowed drainage fluids to exit the sample at the base via a separate tube to prevent H_2 or helium being reinjected during the imbibition cycle [18]. The imbibition fluids exited through the top of the core. The confining pressure and flow were controlled using four syringe pumps (Teledyne ISCO, USA; models 500D and 100DX). The pressure across the mini core was measured at either end of the core holder using a differential pressure transducer (Keller, CH; PD-33X).

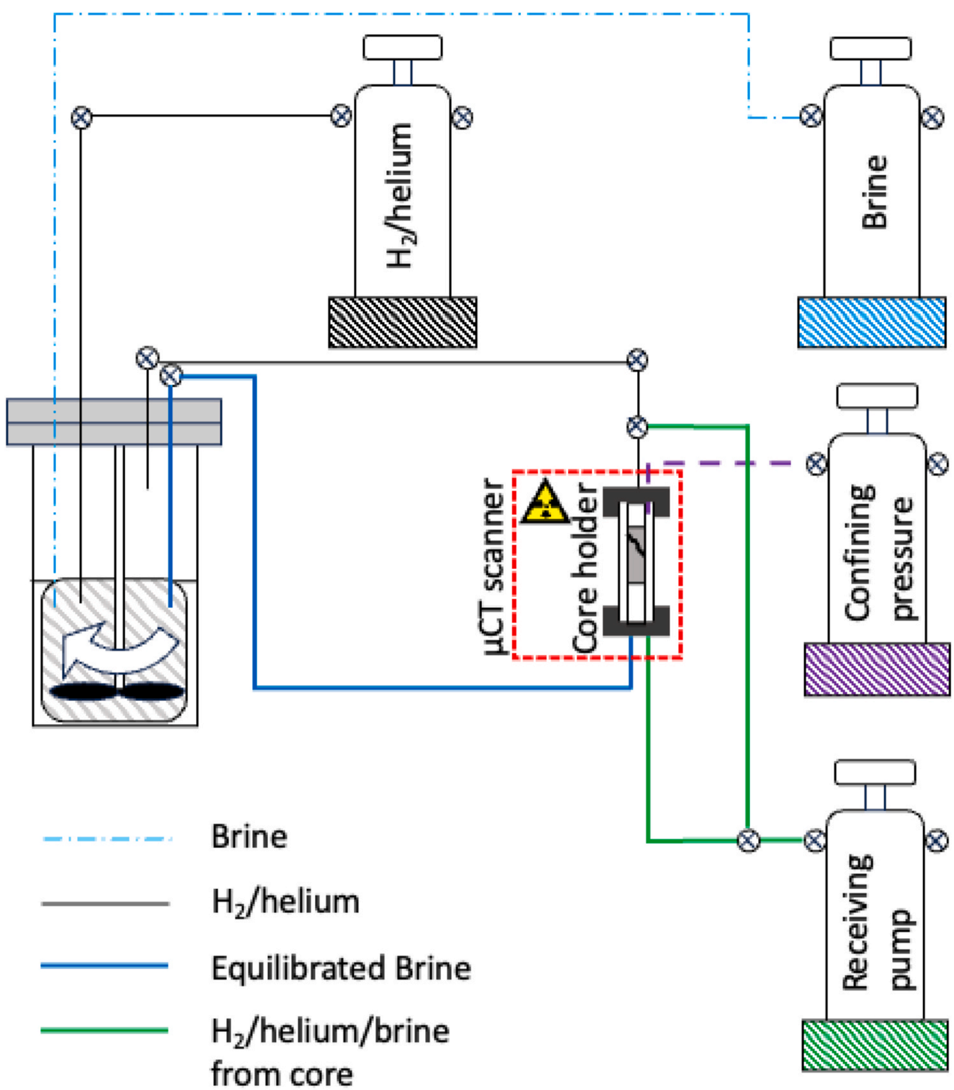

Fig. 4. Schematic of the experimental setup. Helium was substituted for H_2 in the second part of the experiment. The figure does not show the heating tape that was fitted to the outside of the core holder or the thermocouple temperature sensor fixed to the Viton sleeve containing the sample in the core holder.

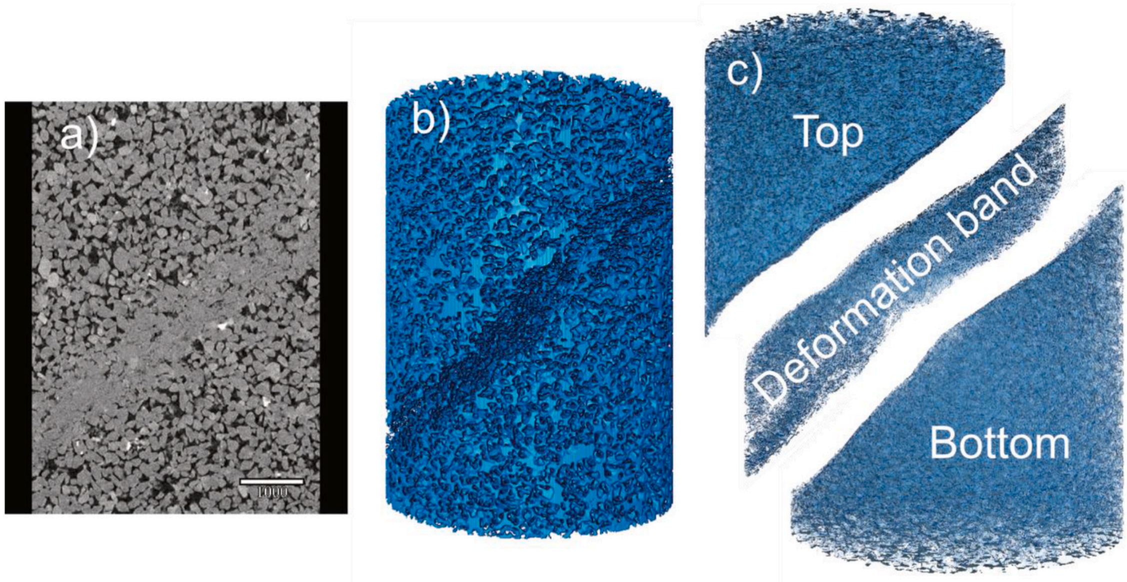

Fig. 5. The three sections, intact rock at the Top, Deformation Band and intact rock at the Bottom. a) 2D greyscale image of one of vertical slices, showing grains (grey) and pores (black), b) a 3D image of the pores and c) a 3D image cut into 3 the sections, showing the pores structure within each section. The extracted image of the sample is 6.4 mm in height.

3.4. Experimental procedure and analysis

Prior to taking an initial dry scan of the sample, we flushed the mini core with CO_2 (BOC, UK; 99.8% purity) to remove air within the pore space. Subsequently, a dry scan was obtained whilst the sample was subjected to 1.5 MPa confining pressure.

Then, the sample was flooded with more than 10 pore volumes of unequilibrated potassium iodide brine and a scan was taken of the brine-flooded sample. For the flooded core scan, the pore pressure was 10 MPa, confining pressure was 11.5 MPa and temperature was 50 °C, as it would be for the drainage and imbibition cycles. The confining and pore pressures were increased in 0.2 MPa steps to allow for stress equilibration, and to prevent mechanical damage to the rock.

3.4.1. H_2-brine injection cycles

Before the injection of H_2, the sample was flooded with more than 10 pore volumes of H_2-equilibrated brine to prevent H_2 dissolution during drainage.

We performed two cycles of H_2 drainage and brine imbibition to determine fluid pathways and hysteretic affects with respect to the deformation band. Initially, H_2 was injected into the brine-saturated core at 0.05 mL min^{-1}, resulting in a capillary number (Ca) of 4.2 x 10^{-9} (Eq (2)).

$$Ca = \frac{\mu v}{\sigma} \quad \text{Eq 2}$$

Under the experimental conditions, H_2 viscosity (μ) is 9.64 x 10^{-6} Pa s, the velocity of the injected H_2 (v) is 2.95 x 10^{-5} m s^{-1} and the interfacial tension (σ) between H_2 and water 0.0683 N m^{-1} [52,53]. Once breakthrough was achieved, determined by the pressure differential signal, the pressure was allowed to stabilise before flow was stopped. Just over 17 pore volumes, or a total of 2.0 ml, of H_2 were injected to achieve this. Once flow was halted, we maintained pressure in the core with the injection pump to stabilise the injected H_2. This was followed by a scan of the sample.

The procedure was then repeated for imbibition, injecting equilibrated brine from the base of the sample at 0.05 mL m^{-1} (Ca = 2.3 x 10^{-7}). Again, flow was stopped following breakthrough and stabilisation of the pressure, and a scan was obtained. Just over 5 pore volumes of brine (0.6 mL) were required to achieve pressure stabilisation following breakthrough.

The drainage and imbibition cycles were repeated, and scans were obtained after each injection. In total, 19 pore volumes of H_2 (2.2 mL) were injected for drainage 2 and nearly 5 pore volumes of brine (0.5 mL) were injected for imbibition 2.

3.4.2. Helium-brine injection cycles

Prior to commencing the cycles with helium, the sample and lines were cleaned with DI water. Then the sample was flooded with helium-equilibrated brine at 50 °C and 10 MPa (again more than 10 pore volumes). A scan of the flooded sample was taken. The same workflow was followed as in the H_2-brine injection cycles. The volumes of helium injected for drainage 1 (D1), imbibition 1 (I1), drainage 2 (D2) and imbibition 2 (I2) are 2.0 mL helium, 0.8 mL brine, 1.7 mL helium and 0.6 mL brine, respectively. The capillary numbers for the helium and brine injections at 0.05 mL min^{-1}, where helium viscosity is 21.28 x 10^{-6} Pa s and helium-brine interfacial tension is 0.068 N m^{-1}, are 9.2 x 10^{-9} and 2.3 x 10^{-7}, respectively [43,44].

3.4.3. Image analysis

The raw data from the CT scans were reconstructed using the EasyTom Xact software. Avizo (2024.1) software (Thermo Fisher Scientific, USA) was then used for image analysis.

Initially, all images were registered to the dry scan, and a cylindrical sub-volume of 4.8 mm diameter and 6.4 mm length (1271 horizontal slices) was extracted as the volume of interest from each of the images. Creating the volume of interest allowed us to remove Teflon tape and aluminium foil from the image. A non-local means filter was applied to all the images to remove noise [54]. The dry image was segmented to differentiate between rock and pore space. This allowed a template of the pore space to be overlaid on each of the images. It was then possible to separate brine and gas within the pore space by further segmentation (Supporting Information A – Image segmentation). Any standalone object of less than 10 voxels, below the resolvable limit, was removed at this point and the volume was incorporated into the surrounding fluid. We performed this step to further refine and reduce the effects of artifacts associated with the imaging and segmentation. The dry and flooded core scan enabled the porosity and connected porosity of the sample to be determined.

Finally, the image was partitioned into three sections: intact rock above the deformation band, intact rock below the deformation band, and the deformation band (Fig. 5). This aided data analysis and enabled us to observe the effects of different rock characteristics on the movement of gas and brine in each section.

4. Results

Here we discuss the results relating to our Sherwood Sandstone sample containing a deformation band (Fig. 5).

4.1. Fluid saturation across the whole sample

The saturations of each fluid after drainage and imbibition cycles are summarised in Table 2. The saturation profiles of the gas phase are displayed in Figs. 6–8. We find similar amounts of H_2 in the sample after D1 and D2. There is little H_2 trapped in the sample after I1; however, there is a substantial increase in trapped H_2 after I2. This equates to a recovery factor of 89% for the first cycle and 71% after the second cycle (Eq (1)), or 85% overall recovery factor after 2 cycles, i.e. total produced H_2 as a proportion of total injected H_2. The helium-brine saturations are comparable to the H_2-brine results after D1 and D2 and the trapped helium increases after I2 (Table 2). However, the trapped helium is higher after I1 and I2, compared to the trapped H_2. As a result, the recovery factor has reduced to 71% after I1 and 55% after the second cycle, or 75% overall recovery factor after 2 cycles.

In addition, Fig. 7 shows that there are few connecting pathways for H_2 across the deformation band in both D1 and D2 and limited H_2 trapped in it after both I1 and I2. A similar observation can be made for helium (Fig. 8).

4.2. Fluid saturation in each section

The distributions of H_2 and helium in Fig. 6 are summarised in Table 3. Comparing the drainage injections, the saturation of H_2 and helium reduce in the top and deformation band after D2 and increase in the bottom section, although most saturations between D1 and D2 (apart from the helium in the top section) are comparable. The amount of H_2 remaining in all three sections after I2 is significantly higher than after I1. Almost all H_2 is displaced from the bottom and deformation band sections after I1 and only 10.9% of H_2 remains in the top section, whereas an additional 6.3%, 7.0% and 8.6% remains trapped in the bottom, deformation band and top sections, respectively after I2. For the helium experiment, there is a similar saturation of helium in the top section after I2, but the amount of gas trapped in the bottom section and deformation band has increased by 8.3% and 4.2%, respectively, in comparison to I1.

The distribution of pore throats is the controlling geometry within the sample [55]. By comparing the pore throat distributions (black lines in Fig. 9a–c and Fig. 10a–c) with the throats occupied by H_2 and helium after each injection, it can be seen that both H_2 and helium inhabit the larger pore throats.

5. Discussion

We prioritise the H_2-brine results as this is the focus of prior research and our study. The helium-brine outcomes will be used as a reference for the H_2-brine results, except in the subsection where we specifically deal with helium as a proxy for H_2. In addition, we recognise that our results are from an experiment on a single cataclastic deformation band and that there may be important differences in comparison with other bands, including lithologies with different sedimentological or diagenetic characteristics. Any upscaled fluid behaviour in relation to deformation bands are based upon inferences from our experiment and relevant literature.

The occupation of the larger pore throats by H_2 and helium confirms that the system is water-wet, as expected in a quartz-rich sandstone [17]. In addition, although the pore throat distribution is similar for the top and bottom sections (Fig. 3), H_2 occupies the smaller throats in the top section after drainage (Fig. 11). This suggests that as the gas reaches the deformation band it is forced into the smaller throats before it can flow through the deformation band.

Despite the inclusion of the deformation band in the sample, the endpoint H_2 saturation is nearly 44% after primary drainage. This saturation is within the range of H_2-brine injection experiments into homogeneous sandstone [47,56,57] and compares favourably with studies utilising samples containing low porosity bands [17,18]. The capillary numbers for these previous experiments range from 2.92 x 10^{-7} to 2.49 x 10^{-10} for drainage and 2.92 x 10^{-5} to 3.68 x 10^{-8} for imbibition. The relatively high H_2 saturation in our sample, for rock containing a low porosity layer, may be due to the high permeability of the intact rock ($>10^{-12}$ m^2 or >1 D). However, H_2 is not distributed evenly throughout the sample, with most remaining in the top section, showing that this deformation band presents a baffle to flow (see Table 3).

There is a similar overall H_2 saturation in the sample after D2 (42%), and again there is uneven distribution, albeit the composition is slightly different compared to D1. The helium results confirm that the deformation band is an obstacle, albeit the difference between the saturation in the top and bottom sections are less marked in drainage.

We observe a low residual H_2 saturation of 4.9% after I1 and almost no H_2 is trapped in the deformation band and bottom section. The pattern of H_2 reduction in the bottom section may be consistent with dissolution, as seemingly this is the H_2 the brine encounters first. Dissolution could account for the H_2 reduction if the brine was unsaturated and could interface with a significant proportion of H_2 in the sample during and post imbibition [58]. Nevertheless, the brine was pre-equilibrated and had already passed through about 8 mm of sample containing H_2 before reaching the imaged section. Additionally, we did not observe the same marked reduction in I2. Therefore, it seems more likely that most H_2 is displaced into the top section or produced at the top of the sample, and that dissolution may only be partly responsible for the absence of H_2, as seen by Boon et al. [59]. The low residual gas after I1 agrees with results from Al-Yaseri et al. [60] who observed low H_2, CO_2 and CH_4 residuals of <10% in a Bentheimer sandstone sample. In addition, the two studies containing low porosity bands [17,18] found that less than 20% of H_2 was trapped after I1. Therefore, despite the difference in depositional settings of the tested sandstones, the outcomes are similar. However, care needs to be taken when extrapolating the results to predict behaviour at the reservoir-scale as small differences at the experimental scale may become significant.

As with previous studies, we find that there is hysteresis in the non-wetting phase (H_2 and helium) [17,57,59]. Trapped H_2 increases in all three sections by 6.3% to 8.6% after I2, to which the deformation band contributes (see below). This is as opposed to the wetting phase (brine), which produces similar saturations after the two drainage cycles. These results suggest that multiple experimental injection-production sequences are needed to understand hysteresis within the system and predict how a reservoir will perform over repeated cycles.

The obstacle the deformation band presents is also apparent from pressure differential data. When the non-wetting fluid reaches the deformation band there is a spike in the pressure required for the fluid to

Table 2
Saturation of phases in the sample in both the H_2-brine and helium-brine experiments after each injection.

	H_2	Brine	Helium	Brine
Drainage1	43.8%	56.2%	40.7%	59.3%
Imbibition1	4.9%	95.1%	11.9%	88.1%
Drainage2	42.0%	58.0%	37.5%	62.5%
Imbibition2	12.2%	87.8%	16.8%	83.2%

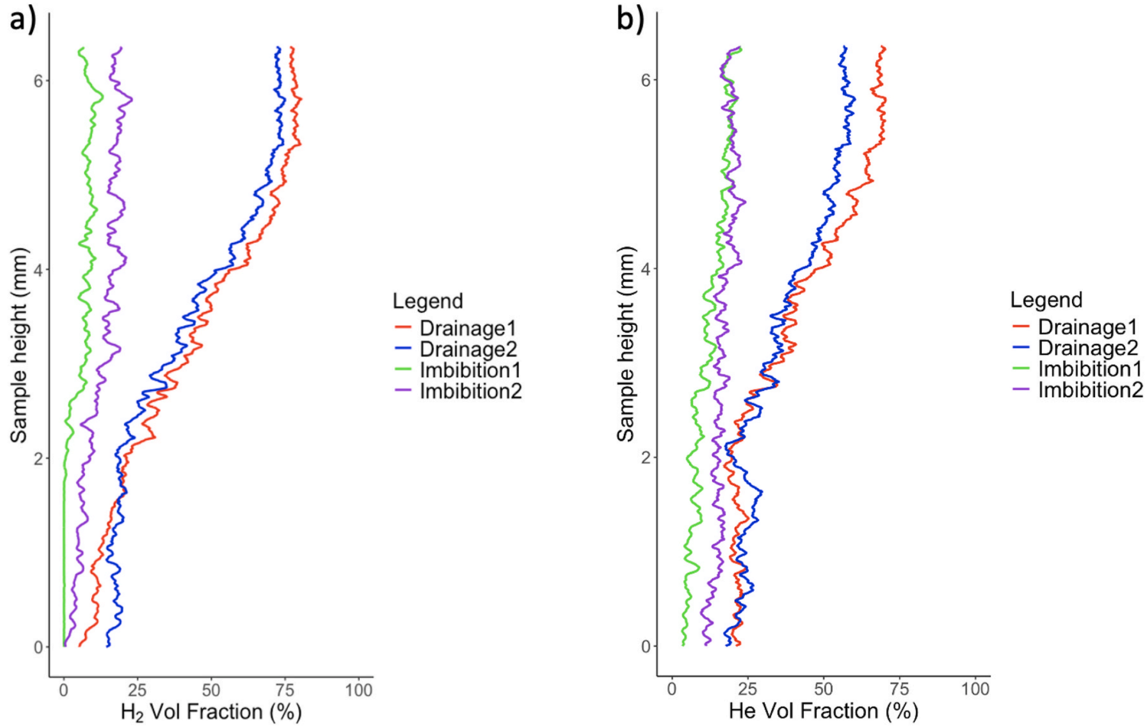

Fig. 6. Saturation profiles of a) H_2 and b) helium after each injection. The gases were injected from the top of the sample (drainage) and the brine from the base (imbibition).

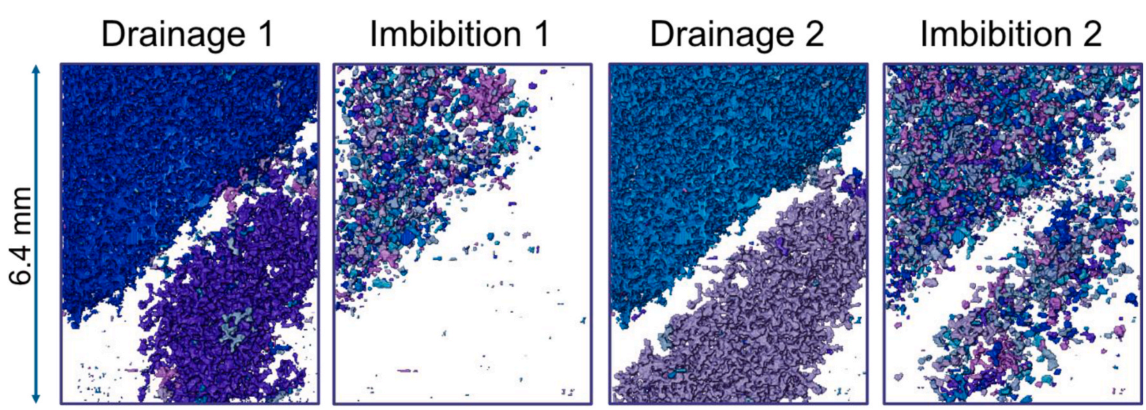

Fig. 7. H_2 in the sample after each injection. The different colours show the different connected H_2 clusters. (For interpretation of the references to colour in this figure legend, the reader is referred to the Web version of this article.)

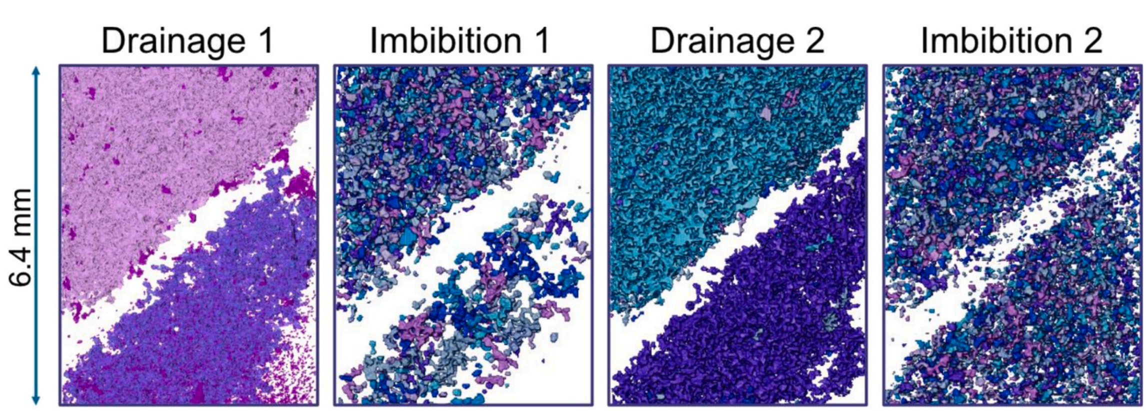

Fig. 8. Helium in the sample after each injection. The different colours show the different connected helium clusters. (For interpretation of the references to colour in this figure legend, the reader is referred to the Web version of this article.)

Table 3
H_2 and helium distribution in each section after each injection.

	D1	I1	D2	I2
H_2				
Top	75.6%	10.9%	71.6%	19.5%
Deformation band	36.4%	0.3%	31.6%	7.3%
Bottom	16.7%	0.1%	18.1%	6.4%
Helium				
Top	67.4%	19.9%	57.1%	21.0%
Deformation band	26.3%	6.8%	23.3%	11.0%
Bottom	21.4%	6.3%	24.3%	14.6%

enter the lower permeability zone, peaking prior to breakthrough. This is the same for both H_2 and helium (see Supporting Information B – Differential pressure measurements). The time taken for H_2 and helium to reach the peak pressure differential, when the fluids are entering the smaller pore throats in the deformation band, from their initial entry into the sample and the magnitude of the pressure differential are also similar for both fluids. This is as expected as the interfacial tensions between the gases and brine are similar at experimental conditions (68 $mN.m^{-1}$). Using the Young-Laplace equation (Eq (3)), describing the relationship between capillary pressure (P_c), interfacial tension between the fluids (σ), the wetting angle (θ) and the pore throat radius, it can be seen that fluids with lower interfacial tension, such as CO_2 and CH_4 [43,61] will require lower pressure to enter the smaller pore throats in the deformation band.

$$P_c = \frac{2\sigma \cos\theta}{r} \quad \text{Eq 3}$$

As stated earlier, the porosity, permeability and thickness of the cataclasis along the deformation band is variable. As the thickness of the deformation band increases it will have a greater impact upon fluid flow; Darcy flow is inversely proportional to length i.e. the width of the deformation band [29]. Likewise, as the permeability contrast between a deformation band and host rock increases above three orders of magnitude there is more likely to be an effect on flow [8,29]. Conversely, there may be points in the deformation band where it is easier for the fluid to traverse, due to increased permeability or a reduction in thickness. However, the average thickness of the band may be more important in determining the impact at metre-scale [62].

5.1. Gas movement – pathways

Our results show that some of the pathways across the deformation

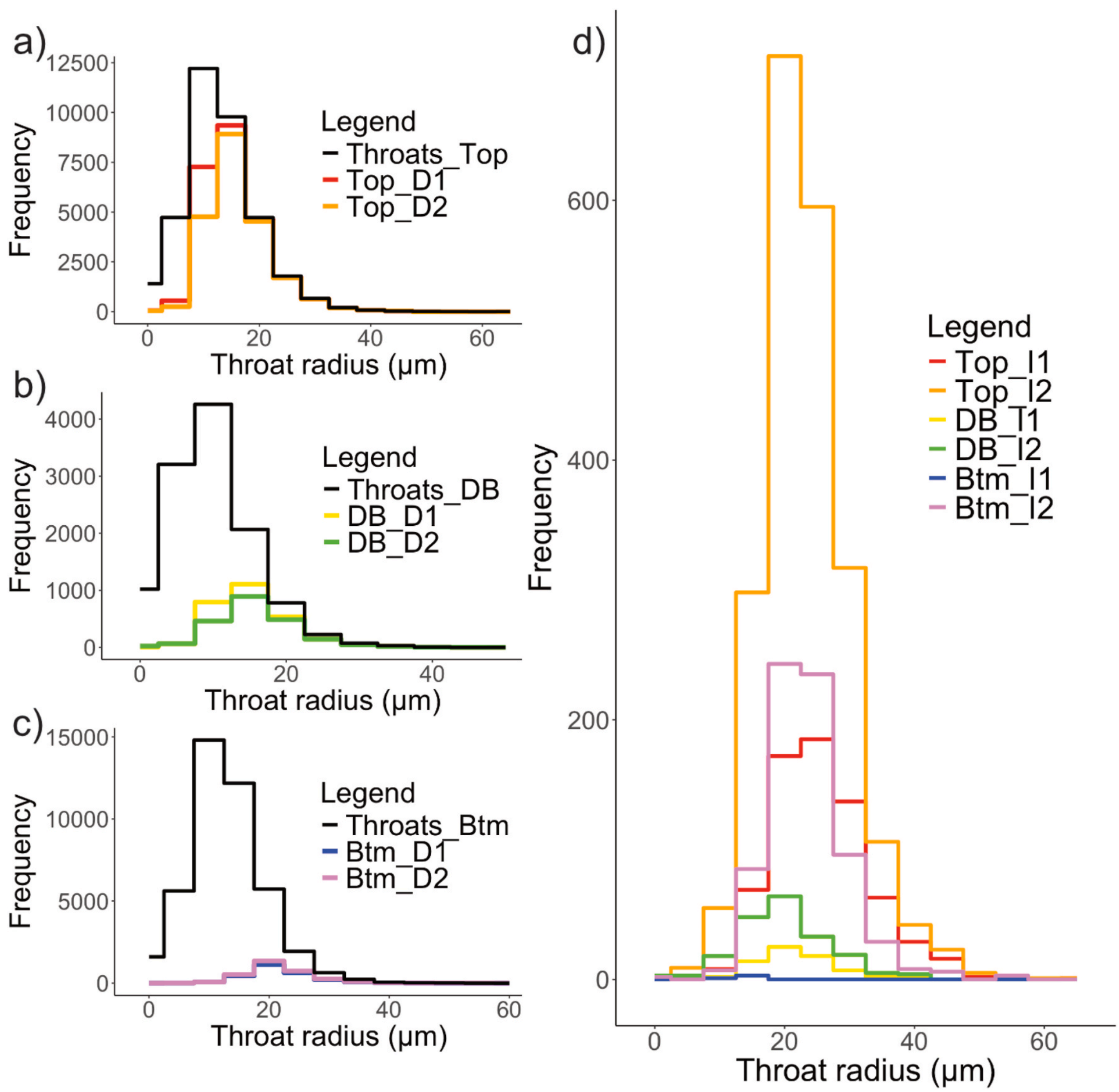

Fig. 9. Distribution of throats occupied by H_2 after each drainage injection (D1 and D2) in a) top section, b) deformation band, c) bottom section and d) all 3 sections after imbibition (I1 and I2). The black line in a-c shows the throat distribution in each section.

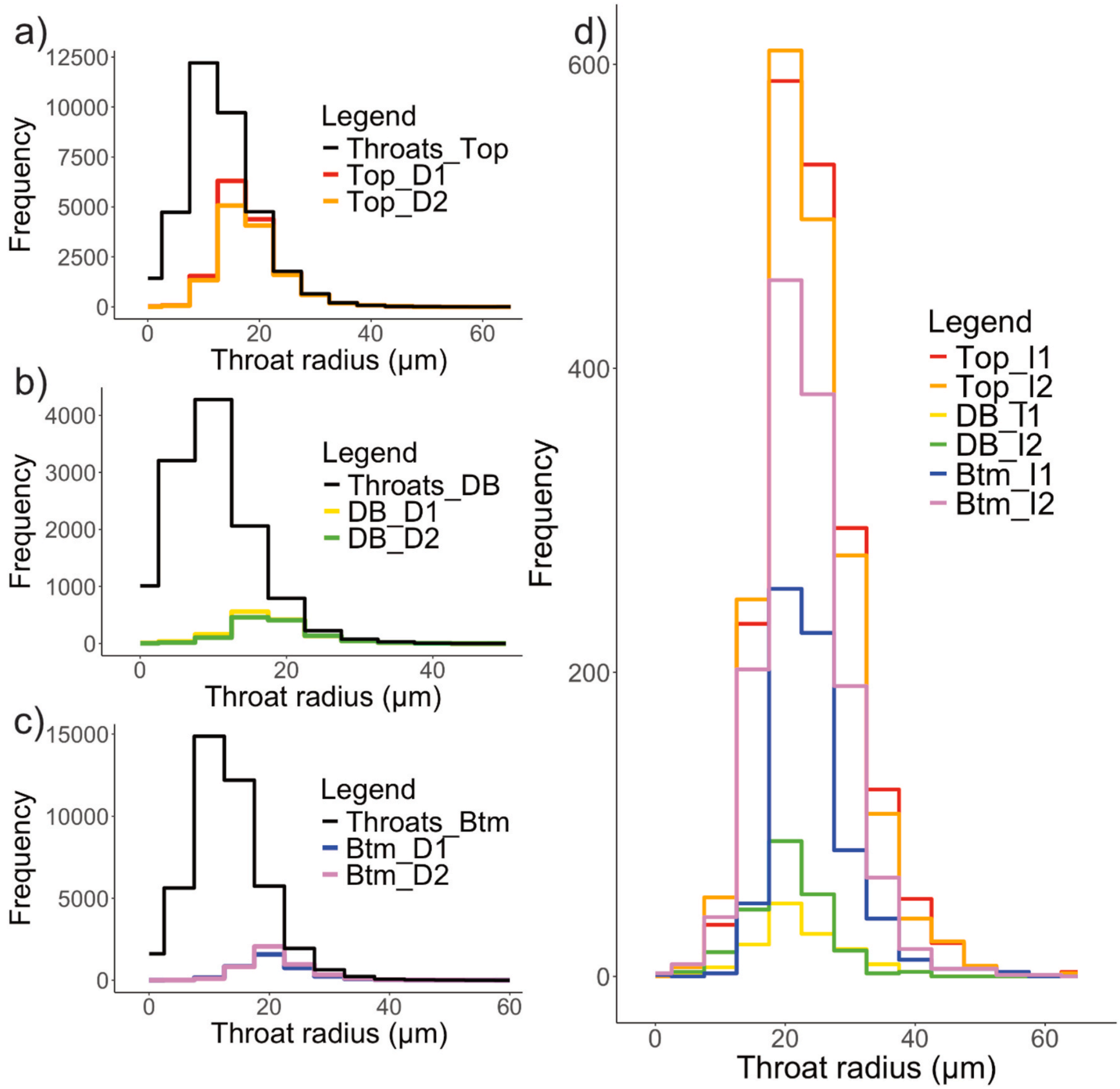

Fig. 10. Distribution of throats occupied by helium after each drainage injection (D1 and D2) in a) top section, b) deformation band, c) bottom section and d) all 3 sections after imbibition (I1 and I2). The black line in a-c shows the throat distribution in each section.

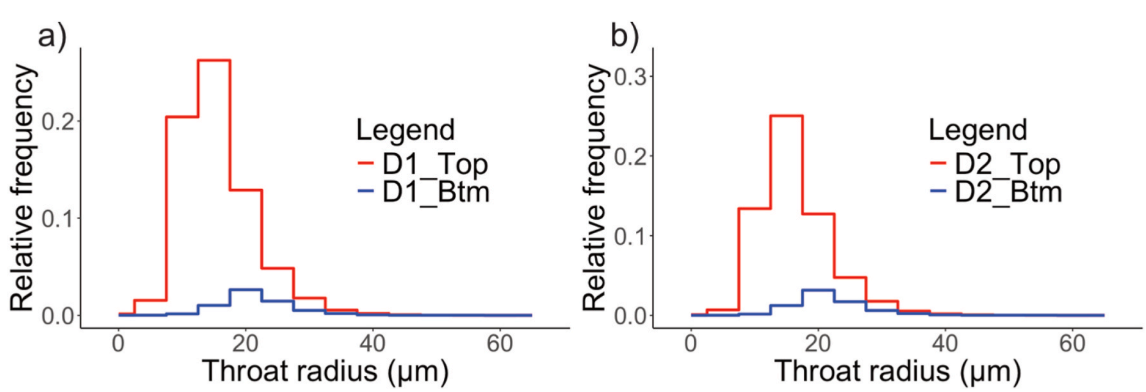

Fig. 11. H_2 distribution in pore throats in top and bottom section after a) drainage 1 (D1) and b) drainage 2 (D2).

band become blocked during the H_2 recovery phase, contributing to H_2 trapping both below and above the deformation band. As there are a limited number of H_2 pathways across the deformation band, where the porosity and permeability is generally reduced (Fig. 5), blockages have a disproportionate effect on flow through the sample. The blockages are a consequence of wetting phase (brine) flow along the surface layer and corners of the pores and throats, eventually swelling to meet (snap off) at the narrowest points (throats) [63]. This process immobilises the H_2 in the larger pore spaces, at least in the short-term.

There are two general areas (viewed from the XY direction) where H_2

is retained in the deformation band after D1 and D2 (Supporting Information D – Gas movement – pathways). It can be inferred that these areas contain the main H_2 pathways through the deformation band. There may also be pathways that are below the image resolution; calculations using pressure data suggest that smallest pore throats entered by H_2 were just under 15 μm diameter, which is below image resolution.

One of the main pathways used in D1 and D2 (Fig. 12c) becomes blocked in I2 producing additional trapping (Fig. 12). The blockage has a knock-on effect beyond the deformation band and the trapped H_2 extends into the pore space below the deformation band (Fig. 12f). It is likely that the blockage contributes to the increase in trapped H_2 in the bottom section after I2.

It is impossible to quantify the effect of this obstruction, due to the combination of other blockages and the utilisation of different pathways in D2. However, its use in the transportation of H_2, and its effect on trapping, can be inferred from visualisations of D2 and I2 (Fig. 13). Brine can transit the pore (highlighted in Fig. 12c) in I1, allowing H_2 to flow through it. However, in I2 the pore is blocked, resulting in H_2 becoming trapped in generally the same volumes and pores in the bottom section that it occupies after D2 (compare Fig. 13a and b with c and d), although there is some movement at the pore-scale (see below). It is unlikely that all the trapping is due to the highlighted pore. The increased H_2 breakthrough to the bottom section in D2 is likely to lead to additional trapping (compared to I1) and there are other pores in the deformation band where H_2 gets trapped that behave similarly to those highlighted in Figs. 12c and 13, also contributing to H_2 trapping in the bottom section.

The blocked pathways in the deformation band and the bottom section also seem to affect trapping in the top section. This is because the blockages reduce the number of pathways available to the brine, which bypasses H_2, trapping more in the top section after I2 (Fig. 14).

The helium-brine drainage results are similar but with higher gas saturation in the deformation band after D1 and D2 (Supporting Information D – Gas movement – pathways). However, many of the pathways used in both drainage injections are still within the two zones (dotted black ellipses in Supplementary Figure 8c). The imbibition comparison is less clear as clusters of trapped helium are scattered throughout the deformation band (Fig. 15) and there is more gas trapped after both imbibition injections. Helium is only trapped in parts of the pore at the base of the deformation band (Fig. 15c and f, highlighted in the H_2 experiment in Fig. 12c and f), seemingly enabling brine to transit the pore in both I1 and I2, albeit in a reduced manner.

5.2. Gas movement – pores

After I2, H_2 is trapped in the centre of larger pores that were previously filled with brine after D2 (Supporting Information E – Gas movement – pores). We expected brine injection in I2 to displace H_2, particularly from pathways with smaller pore throats [57], which would be produced at the top of the sample in our experiment. However, the movement of H_2 into the centre of pores was not anticipated. This indicates post injection movement of H_2 or the exsolution of H_2 due to local pressure effects within the sample, as observed by Boon et al. [59]. We only observe this behaviour in the bottom and deformation band sections, although this could be due to higher H_2 saturation in the top section after both D2 and I2, offering fewer opportunities for H_2 to move into previously brine-filled spaces and making it harder to observe. In the top section, also after I2, we observe H_2 trapping in the centre of some of the larger pores, surrounded by brine [57]. These pores were filled with H_2 after D2.

Helium behaves similarly. There is gas movement into pore centres in the bottom and deformation band sections after D2 and bypassing of the helium within the large pores in the top section (Supporting Information E – Gas movement – pores).

5.3. Comparison between H_2 and helium

There are many similarities in the behaviour of H_2 and helium across the two cycles of drainage and imbibition. The similarities include the overall saturation, with similar outcomes for D1 and D2 and more trapping after I2 (Table 2). Residual helium saturation after imbibition is

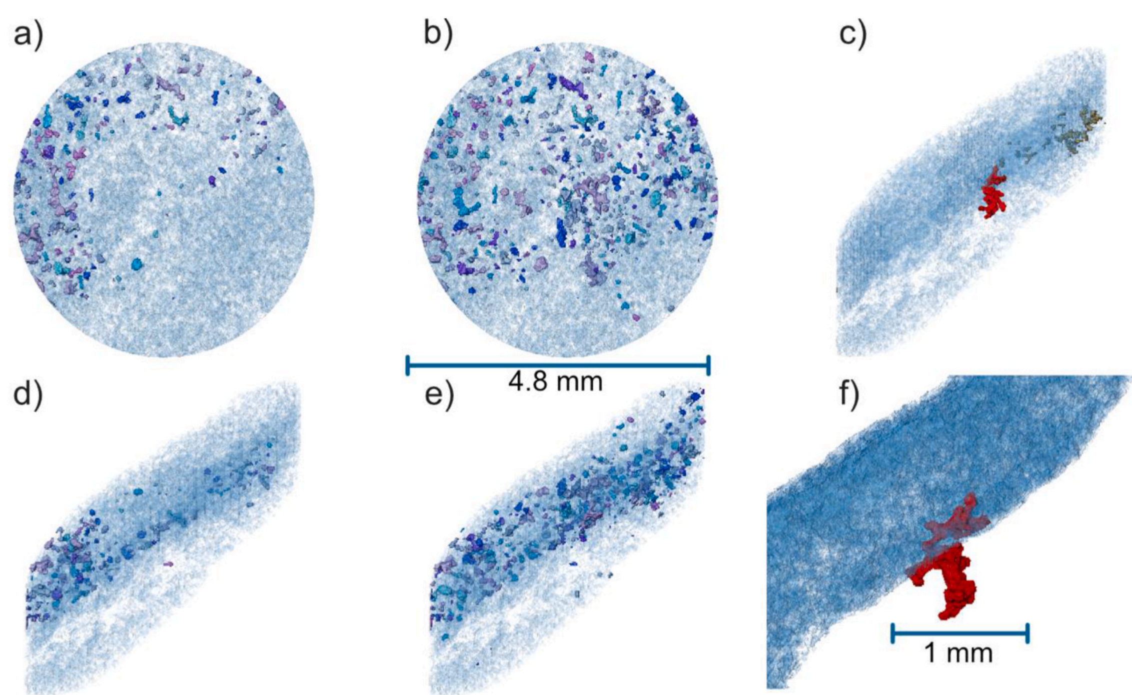

Fig. 12. H_2 trapped in the deformation band after a) I1 and b) I2. a) and b) show the plan (XY) view; d) and e) show the corresponding XZ view. c) shows H_2 trapped after I2 in pores that are also used in both D1 and D2, with f) an expanded view of the largest blockage, continuing into the bottom section. The light blue lines show the pore network in the deformation band. The other colours show the different H_2 clusters. (For interpretation of the references to colour in this figure legend, the reader is referred to the Web version of this article.)

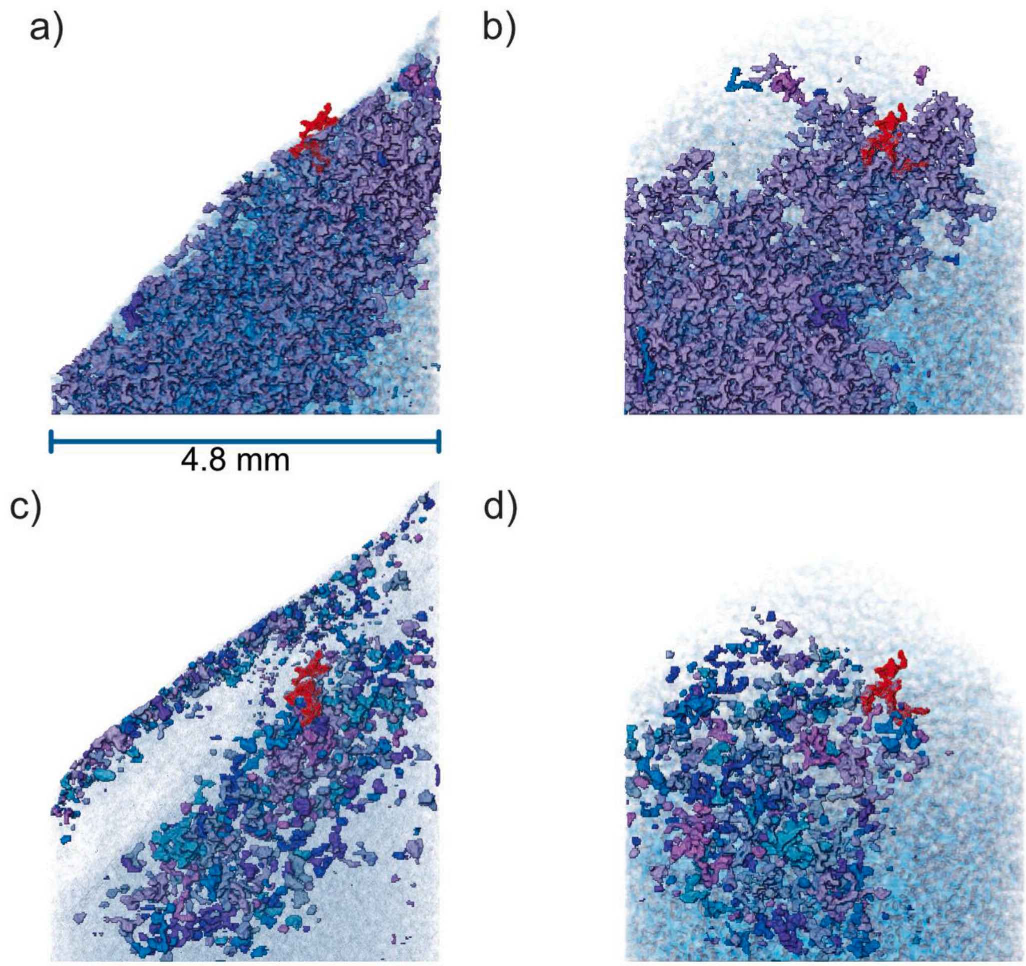

Fig. 13. H_2 in the bottom section of the sample after D2 in a) XZ view; b) rotated XZ view. H_2 trapped in sample after I2 in c) the deformation band and the bottom section in XZ view and d) the bottom section in a rotated XZ view. The highlighted pore (red) is used in both drainage injections and contains trapped H_2 after I2. Light blue shows the pore network of the bottom section (and deformation band in c). The other colours show H_2 clusters. (For interpretation of the references to colour in this figure legend, the reader is referred to the Web version of this article.)

also more comparable with H_2 than results for N_2 [39]. Additionally, the profile and magnitude of the pressure differential and the time taken for gas to break through the deformation band are similar (Supporting Information B – Differential pressure measurements). There is some difference in the pressure signals after breakthrough, but these are within the accuracy tolerance of the pressure transducer ($\pm$0.15 bar).

The pattern of saturation across the sample is also similar, with higher gas saturations in the top section after drainage and imbibition injections. However, more helium breaks through to the bottom section after both drainage injections and, as a likely consequence of this, becomes trapped beneath the deformation band after imbibition (Table 3). This may be due to the viscosity of helium being twice as high as for H_2, indicating that the capillary forces have a slightly lower influence on flow across the deformation band. Adjusting the capillary number by reducing the helium flow rate, may reduce these differences. Despite the increase in breakthrough for helium, the throat occupancy profile is similar for both gases after both drainage and imbibition (Supporting Information C – Throat occupancy after each injection).

The gases appear to behave similarly within the pores, displaying movement between D2 and I2 in the bottom and deformation band sections. This indicates that there may be similar redistribution processes, not found with nitrogen [37], although there was no appreciable no-flow period in our experiments. In addition, in the top section, there is gas trapping in the centre of larger pores due to snap-off during imbibition, in respect of both gases.

Therefore, within our experimental parameters, the results suggest that it is possible to use helium as a proxy for H_2 in laboratory pore-scale experiments. However, caution may be needed if helium is used to quantify the efficacy of H_2 storage, i.e. by using helium as a proxy to calculate the recovery factor.

5.4. *Effects on the reservoir scale*

In this section we make some observations about the potential impact of deformation bands at a scale applicable to UHS. These are based on the results of our experiment coupled with findings from the wider literature concerning the structure of deformation bands and fluid behaviour in relation to them. We focus on capillary effects, which are enhanced in deformation bands, where narrower pore throats increase fluid–rock interaction.

In UHS, capillary effects are more likely to dominate viscous flow towards the fringes of the H_2 plume (i.e. at the interface of the fluids, in the mixing zone), where H_2 saturation is low and the pressure gradient, and therefore the capillary number, is reduced. Under these conditions, capillary entry pressure controls H_2 flow into deformation bands [29].

The orientation of deformation bands further affects fluid flow. Unlike many other permeability contrasts related to primary sedimentation, such as laminations, deformation bands are often oblique to bedding [27], and flow is therefore preferentially diverted parallel to their long axes [64]. In this study, fluids were forced to interact with a

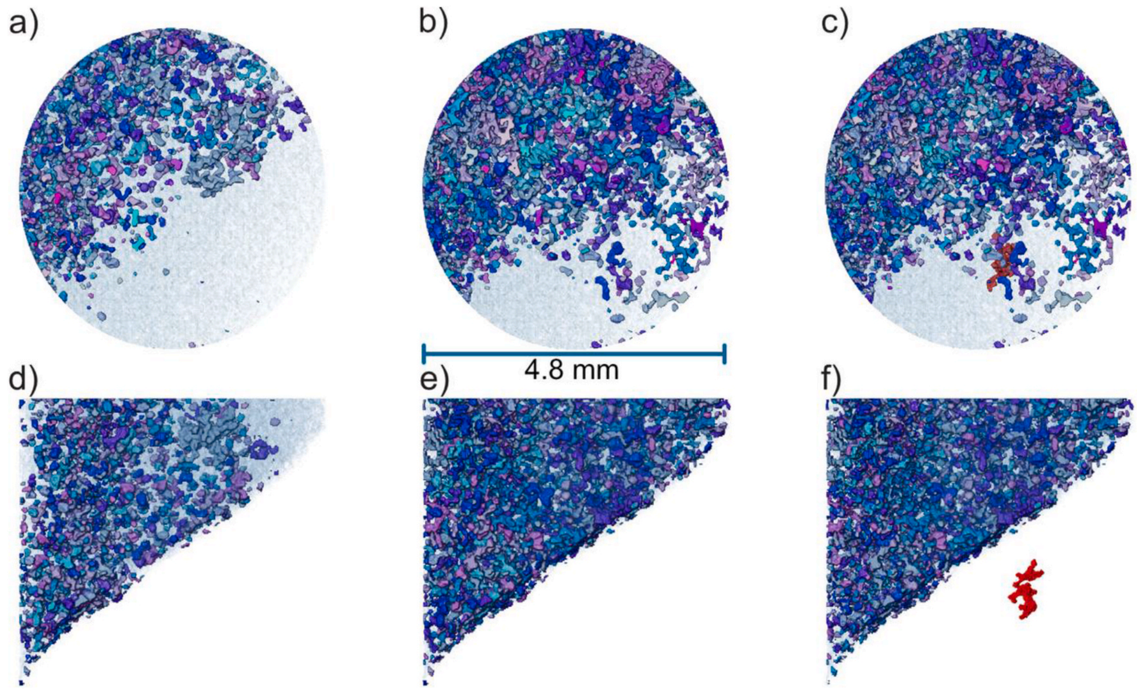

Fig. 14. H_2 remaining in the top section after imbibition. a) I1 and b) I2 and c) the additional H_2 that is trapped after I2 (but not after I1). The top images show the plan (XY) view and the lower images (d – f) show the XZ view. c) and f) also shows the position of the pore (red) that traps H_2 after I2 (but not I1). The light blue lines show the pore network in the deformation band. The other colours show the H_2 clusters. (For interpretation of the references to colour in this figure legend, the reader is referred to the Web version of this article.)

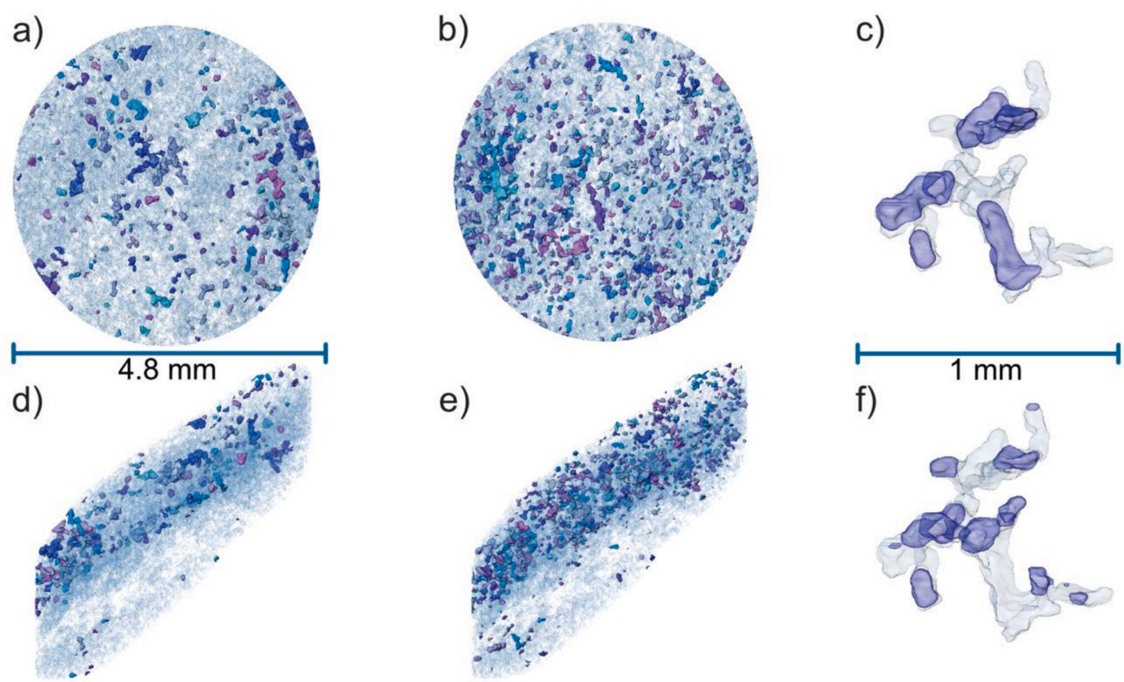

Fig. 15. Helium trapped in the deformation band after a) I1 and b) I2. The top images (a and b) show the plan (XY) view, and the lower images (d and e) show the XZ view. c) and f) show the helium trapped in the at the bottom of the deformation band (Fig. 12) after I1 and I2, respectively. Light blue lines show the pore network in the deformation band. Other colours show the helium clusters. (For interpretation of the references to colour in this figure legend, the reader is referred to the Web version of this article.)

deformation band, and the main H_2 pathways were observed in the vertically higher part of the feature (when viewed in the XZ direction, to the right in Fig. 7). This suggests that the upper portion of the band is more accessible as a consequence of localised pressure gradients. For example, during imbibition there is a higher pressure below the part of the band closer to the top of the sample due to the increased gas column height beneath it [8]. At the reservoir scale, the greatest effect of single deformation bands is therefore likely to be redirection of flow, potentially dispersing the plume [29].

Deformation bands may occur as clusters, in which case they can exhibit a more pronounced permeability contrast and have been shown to act as seals in hydrocarbon reservoirs ([29]; Tueckmantal et al., 2012; [11]). Therefore, deformation bands may cause fluids to be diverted and follow a more tortuous pathway or become trapped [22,29,64,65]. Clusters are expected to exert a greater influence on UHS by having a more pronounced effect on flow paths and fluid trapping, potentially reducing effective storage capacity and overall reservoir performance [65]. Investigating the impact of deformation band clusters on UHS therefore represents a logical extension of this study.

Both individual deformation bands and clusters may compartmentalise the reservoir. In such cases, their effects are aggregated, trapping H_2 beneath baffles, controlling brine pathways, and modifying localised pressure gradients [8,65]. Consequently, H_2 may become temporarily immobilised below, within, or above a compartment, increasing its exposure to dissolution [59] and reducing plume coherence. These processes would be expected to negatively affect fluid injection, recovery factor and reservoir capacity [65].

However, immobilisation is not necessarily permanent: H_2 may become reconnected during shut-in periods as a result of post-injection redistribution driven by local pressure changes, including buoyancy effects or Ostwald ripening, or during subsequent injection cycles [66–71]. Reconnection may also be facilitated by increasing the flow rate during drainage, provided formation mechanics allow an increase in pressure gradient [72]. In combination, these mechanisms have been shown experimentally to improve UHS recovery efficiency over multiple cycles [70] and are consistent with UHS simulations (e.g. Ref. [73]).

While deformation bands are unlikely to render a reservoir unusable, awareness of their potential effects is important, particularly in storage sites where such features are present and operating pressures are low. Recognising these impacts allows reservoir engineers to anticipate potential issues and implement appropriate mitigation strategies during reservoir modelling and operation. However, further work is needed to scale up experimental results.

One potential mitigation strategy to reduce cost and increase storage efficiency involves the use of alternative cushion gases such as CO_2, CH_4, or N_2, which have been shown to reduce the interfacial tension between H_2 and brine [53,74,75]. Reduced interfacial tension would lower capillary entry pressures into narrow pore throats (Eq (3)), decreasing the energy required for H_2 to flow through deformation bands and reducing the likelihood of trapping. However, this approach may reduce produced H_2 purity, promote unwanted biochemical reactions, and increase the risk of caprock permeation due to the lower interfacial tension [76].

6. Conclusion

To better understand the effect of deformation bands on UHS we performed two cycles of H_2 injection (drainage) and production (imbibition) on a Sherwood Sandstone sample containing a deformation band. The permeability of the deformation band was three orders of magnitude lower than the surrounding intact rock. The experiment recreated a capillary-dominated regime at reservoir conditions of 50 °C and 10 MPa, to observe the effect of permeability contrasts on fluid movement. In addition, we performed the same analysis with helium to further evaluate the effect of the permeability contrasts and determine whether helium is a useful proxy for H_2.

Our main findings are.

- The deformation band acts as a baffle to flow with reduced transecting pathways compared to undeformed rock. The barrier forces gas into smaller pore throats than would otherwise be occupied, before transiting the deformation band.
- We observe almost no trapping in and below the deformation band after the first imbibition for the H_2 experiment. However, once there is a blockage, created by snap-off of the wetting fluid (brine), H_2 trapping substantially increases. The blockage causes H_2 to become trapped, both below and above the deformation band, reducing H_2 production. Therefore, we find that deformation bands can reduce the H_2 recovery factor from a reservoir.
- There is hysteresis in the non-wetting phase; the deformation band likely increases this effect due to additional trapping. We did not find hysteresis for the wetting phase, although there was a change in brine distribution after each drainage injection. Consequently, it is necessary to perform multiple injection-production cycles to understand the behaviour of H_2 in relation to UHS.
- After drainage there is movement of H_2 between pores in the bottom and deformation band sections of the sample, where H_2 saturation is lower. Here, H_2 moves into the centre of pores, previously occupied by brine immediately after drainage. In the top section, where H_2 saturation is higher, there is trapping of H_2 in the centre of pores after imbibition. We observe both processes in larger pores with brine occupying the surfaces of the pore. Therefore, multiple processes contribute to H_2 trapping in the sample, reducing reservoir efficiency at least temporarily. However, trapped H_2 may become reconnected in subsequent H_2 injections or in post-injection processes, such as Ostwald ripening or buoyancy effects.
- There are many similarities between the behaviour of H_2 and helium under the current experimental conditions, which mimic certain reservoir settings. As such, helium could be used as a proxy in these situations, providing additional experimental design options. Similarities include the overall saturation pattern, the pressure measurements (pressure profile, time to breakthrough and pressure differential needed for breakthrough), pore throat distribution and the movement of gases after drainage 2. However, the viscosity difference may reduce the capillary pressure effects, which needs further exploration in future research.

Overall, it is important to understand the effect that deformation bands can have on the efficacy of UHS as there will be some localised pressure effects and H_2 losses, at least temporarily, as a result of their presence. However, the effects are likely to occur away from the wells, in the mixing zone, where the pressure gradient is reduced. In addition, a combination of post-injection mechanisms, allowing trapped H_2 to reconnect, appropriate reservoir pressure management and the cyclicity of UHS should minimise the deformation bands' impact upon reservoir efficacy.

Data

Images from the μCT scans can be found online at https://doi.org/10.5281/zenodo.18284122.

CRediT authorship contribution statement

Douglas Smith: Conceptualization, Data curation, Formal analysis, Funding acquisition, Investigation, Methodology, Project administration, Visualization, Writing – original draft, Writing – review & editing. **Edward Hough:** Supervision, Writing – review & editing. **Daniel Arnold:** Supervision, Writing – review & editing. **Oliver Wakefield:** Supervision, Writing – review & editing. **Zaid Jangda:** Methodology, Visualization, Writing – review & editing. **Kamaljit Singh:** Methodology, Resources, Supervision, Visualization, Writing – review & editing. **Andreas Busch:** Resources, Supervision, Writing – review & editing.

Declaration of competing interest

The authors declare that they have no known competing financial interests or personal relationships that could have appeared to influence the work reported in this paper.

Acknowledgements

The authors would like to thank Nick Harpers, Jeremy Rushton, Sajjad Foroughi and the National Geological Repository for their assistance with data gathering and interpretation. This work was supported by the Natural Environment Research Council via an IAPETUS2 PhD studentship held by D Smith (grant reference NE/S007431/1). E Hough and O Wakefield publish with the permission of the Executive Director, British Geological Survey (UKRI).

Appendix A. Supplementary data

Supplementary data to this article can be found online at https://doi.org/10.1016/j.ijhydene.2026.156079.

References

[1] Clarke L, Wei Y-M, De La Vega Navarro A, Garg A, Hahmann AN, Khennas S, Azevedo IML, Löschel A, Singh AK, Steg L, Strbac G, Wada K. Energy systems. In: Shukla PR, Skea J, Slade R, Al Khourdajie A, van Diemen R, McCollum D, Pathak M, Some S, Vyas P, Fradera R, Belkacemi M, Hasija A, Lisboa G, Luz S, Malley J, editors. IPCC, 2022: climate change 2022: mitigation of climate Change. Contribution of Working Group III to the sixth assessment report of the intergovernmental Panel on climate change. Cambridge, UK and New York, NY, USA: Cambridge University Press; 2022. https://doi.org/10.1017/9781009157926.008. https://www.ipcc.ch/report/ar6/wg3/downloads/report/IPCC_AR6_WGIII_Chapter06.pdf.

[2] IEA. Global Hydrogen Review 2023 [online], https://www.iea.org/reports/global-hydrogen-review-2023; 2023.

[3] IEA. World energy outlook [online], https://www.iea.org/reports/world-energy-outlook-2024; 2024.

[4] IEA. *Global Hydrogen Review* [online]. https://www.iea.org/reports/global-hydrogen-review-2024; 2024.

[5] Heinemann N, Alcalde J, Miocic JM, Hangx SJT, Kallmeyer J, Ostertag-Henning C, Hassanpouryouzband A, Thaysen EM, Strobel GJ, Schmidt-Hattenberger C, Edlmann K, Wilkinson M, Bentham M, Haszeldine RS, Carbonell R, Rudloff A. Enabling large-scale hydrogen storage in porous media – the scientific challenges. Energy Environ Sci 2021;14:853. 2021.

[6] Hydrogen TCP-Task 42. Underground hydrogen storage: technology monitor report [online], https://www.ieahydrogen.org/tasks-reports/; 2023.

[7] Muhammed NS, Haq B, Al Shehri D, Badmus SO, Adebayo AR, Mahmoud M. Hydrogen injection and withdrawal performance in depleted gas reservoirs. Int J Hydrogen Energy 2024;96:427–42. https://doi.org/10.1016/j.ijhydene.2024.11.229.

[8] Smith D, Arnold D, Hough E, Busch A. *Numerical modelling of the effects of permeability contrasts on underground hydrogen storage in sandstone reservoirs* Geoenergy. https://doi.org/10.1144/geoenergy2023-039; 2024.

[9] Peksa AE, Wolf KAA, Zitha PLJ. Bentheimer sandstone revisited for experimental purposes. Mar Petrol Geol 2015;67:701–19. https://doi.org/10.1016/j.marpetgeo.2015.06.001.

[10] Lawrence A, Stuart M, Cheney C, Jones N, Moss R. Investigating the scale of structural controls on chlorinated hydrocarbon distributions in the fractured-porous unsaturated zone of a sandstone aquifer in the UK. Hydrogeol J 2006;14:1470–82. https://doi.org/10.1007/s10040-006-0068-6. 2006.

[11] Griffiths J, Faulkner DR, Edwards AP, Worden RH. Deformation band development as a function of intrinsic host-rock properties in Triassic Sherwood Sandstone, vol. 435. Geological Society, London, Special Publications; 2016. p. 161–76. https://doi.org/10.1144/SP435.11.

[12] Uliasz-Misiak B, Misiak J, Lewandowska-Śmierzchalska J. Hydrogen storage in porous rocks: a bibliometric analysis of research trends. Energies 2024;17(4):805. https://doi.org/10.3390/en17040805. 2024.

[13] Jadhawar P, Saeed M. Mechanistic evaluation of the reservoir engineering performance for the underground hydrogen storage in a deep North Sea aquifer. Int J Hydrogen Energy 2023;50(Part D):558–74. https://doi.org/10.1016/j.ijhydene.2023.07.272.

[14] Jia C, Ren B, Sepehrnoori K, Delshad M, Liu B, Sun H, Yao J. Numerical studies of hydrogen buoyant flow in storage aquifers. Fuel 2023;349:128755. https://doi.org/10.1016/j.fuel.2023.128755.

[15] Bo Z, Hörning S, Underschultz JR, Garnett A, Hurter S. Effects of geological heterogeneity on gas mixing during underground hydrogen storage (UHS) in braided-fluvial reservoirs. Fuel 2024;357(2024):129949. https://doi.org/10.1016/j.fuel.2023.129949.

[16] Khandoozi S, Li P, Ershadnia R, Dai Z, Zhang Z, Stauffer PH, Mehana M, Cole DR, Soltanian MR. An integrated approach for optimizing geological hydrogen storage. Appl Energy 2025;381:125182. https://doi.org/10.1016/j.apenergy.2024.125182.

[17] Boon M, Hajibeygi H. Experimental characterization of H_2/water multiphase flow in heterogeneous sandstone rock at the core scale relevant for underground hydrogen storage (UHS). Sci Rep 2022;12(2022):14604. https://doi.org/10.1038/s41598-022-18759-8.

[18] Jangda Z, Menke H, Busch A, Geiger S, Bultreys T, Singh K. Subsurface hydrogen storage controlled by small-scale rock heterogeneities. Int J Hydrogen Energy 2024;60:1192–202. https://doi.org/10.1016/j.ijhydene.2024.02.233. 2024.

[19] Allen DJ, Brewerton LJ, Coleby LM, Gibbs BR, Lewis MA, MacDonald AM, Wagstaff SJ, Williams AT. The physical properties of major aquifers in England and Wales. Hydrogeology Group 1997. Technical Report WD/97/34.

[20] Newell A. Rifts, rivers and climate recovery: a new model for the Triassic of England. PGA (Proc Geol Assoc) 2018;129:352–71. https://doi.org/10.1016/j.pgeola.2017.04.001. 2018.

[21] English KL, English JM, Moscardini R, Haughton PDW, Raine RJ, Cooper M. Review of Triassic Sherwood Sandstone Group reservoirs of Ireland and Great Britain and their future role in geoenergy applications. Geoenergy 2024;2(Issue 1). https://doi.org/10.1144/geoenergy2023-042. 2024.

[22] Wakefield OJW, Hough E, Hennissen JAI, Thompson J, Cripps C, Parkes D. Lithofacies control on the formation of deformation bands: an example from the Sherwood Sandstone Group (Induan–Anisian, Lower Triassic) in Western England. AAPG (Am Assoc Pet Geol) Bull 2022;106(6):1301–24. https://doi.org/10.1306/02032218027. 2022.

[23] Cowan G. Identification and significance of aeolian deposits within the dominantly fluvial Sherwood Sandstone Group of the East Irish Sea Basin UK, vol. 73. Geological Society, London, Special Publications; 1993. p. 231–45. https://doi.org/10.1144/GSL.SP.1993.073.01.14.

[24] Bloomfield JP, Moreau MF, Newell AJ. Characterization of permeability distributions in six lithofacies from the Helsby and Wilmslow sandstone formations of the Cheshire Basin, UK, vol. 263. Geological Society, London, Special Publications; 2006. p. 83–101. https://doi.org/10.1144/GSL.SP.2006.263.01.04.

[25] BGS. Single Onshore Borehole Index (SOBI) [online]. https://api.bgs.ac.uk/sobi-scans/v1/borehole/scans/items/151936; 2025.

[26] Fossen H, Schultz RA, Shipton ZA, Mair K. Deformation bands in sandstone: a review. J Geol Soc 2007;164(2007):755–69. https://doi.org/10.1144/0016-76492006-036. London.

[27] Pourmalek A, Newell AJ, Shariatipour SM, Butcher AS, Milodowski AE, Bagheri M, Wood AM. Deformation bands in high-porosity sandstones: do they help or hinder CO_2 migration and storage in geological formations? Int J Greenh Gas Control 2021;107:103292. https://doi.org/10.1016/j.ijggc.2021.103292.

[28] Medici G, Jared West L, Mountney NP, Welch M. Permeability of rock discontinuities and faults in the Triassic Sherwood Sandstone Group (UK): insights for management of fluvio-aeolian aquifers worldwide. Hydrogeol J 2019;27:2835–55. https://doi.org/10.1007/s10040-019-02035-7. 2019.

[29] Fossen H, Bale A. Deformation bands and their influence on fluid flow. AAPG (Am Assoc Pet Geol) Bull 2007;91(12):1685–700. https://doi.org/10.1306/07300706146.

[30] Jackson SJ, Krevor S. Small-Scale capillary heterogeneity linked to rapid plume migration during CO_2 storage. Geophys Res Lett 2020;47. https://doi.org/10.1029/2020GL088616.

[31] Tueckmantel C, Fisher QJ, Grattoni CA, Aplin AC. Single- and two-phase fluid flow properties of cataclastic fault rocks in porous sandstone. Mar Petrol Geol 2012;29:129–42. https://doi.org/10.1016/j.marpetgeo.2011.07.009. 2012.

[32] James A, Bertouche M, Foote N, Hern CY. The value of integrated core-CT-BHI data in characterising aeolian dune geometries and effects of cross-cutting deformation bands - implications for permeability architecture, 527. Geological Society, London, Special Publications; 2022. p. 173–97. https://doi.org/10.1144/SP527-2022-212.

[33] Romano CR, Zahasky C, Garing C, Minto JM, Benson SM, Shipton ZK, Lunn RJ. Subcore Scale fluid flow behavior in a sandstone with cataclastic deformation bands. Water Resour Res 2020;56. https://agupubs.onlinelibrary.wiley.com/doi/full/10.1029/2019WR026715.

[34] Higgs S, Wang YD, Sun C, Ennis-King J, Jackson SJ, Armstrong RT, Mostaghimi P. *Comparative analysis of hydrogen, methane and nitrogen relative permeability: implications for Underground Hydrogen Storage*. J Energy Storage 2023;73(Part C):108827. https://doi.org/10.1016/j.est.2023.108827.

[35] Newell AJ, Shariatipour SM. Linking outcrop analogue with flow simulation to reduce uncertainty in sub-surface carbon capture and storage: an example from the Sherwood Sandstone Group of the Wessex Basin, vol. 436. UK: Geological Society, London, Special Publications; 2016. https://doi.org/10.1144/sp436.2.

[36] Sadeghi S, Sedaee B. Mechanistic simulation of cushion gas and working gas mixing during underground natural gas storage. J Energy Storage 2022;46:103885. https://doi.org/10.1016/j.est.2021.103885.

[37] Song R, Feng D, Hui G, Liu J, Yang C. Visualized experiments on the hydrogen transports and bubble ripening mechanism in porous reservoir of underground hydrogen storage. Int J Hydrogen Energy 2025;105:326–44. https://doi.org/10.1016/j.ijhydene.2025.01.194. 2025.

[38] Manoorkar S, Kalyoncu G, Omar H, Barbaix S, Ceursters D, Latinis M, Offenwert SV, Bultreys T. Pore-scale imaging of hydrogen and methane storage in fractured aquifer rock: the impact of gas type on relative permeability. Adv Water Resour 2025;206:105109. https://doi.org/10.1016/j.advwatres.2025.105109.

[39] Thaysen EM, Butler IB, Hassanpouryouzband A, Freitas D, Alvarez-Borges F, Krevor S, Heinemann N, Atwood R, Edlmann K. Pore-scale imaging of hydrogen displacement and trapping in porous media. Int J Hydrogen Energy 2023;48(8):3091–106. https://doi.org/10.1016/j.ijhydene.2022.10.153.

[40] Bo Z, Boon M, Hajibeygi H, Hurter S. Impact of experimentally measured relative permeability hysteresis on reservoir-scale performance of underground hydrogen storage (UHS). Int J Hydrogen Energy 2023;48(36):13527–42. https://doi.org/10.1016/j.ijhydene.2022.12.270.

[41] Yuan L, Stanley A, Dehghanpour H, Reed A. Measurement of helium diffusion in Lotsberg Salt cores: a proxy to evaluate hydrogen diffusion. Int J Hydrogen Energy 2024;52A:686–702. https://doi.org/10.1016/j.ijhydene.2023.08.003.
[42] K C B, Frash LP, Creasy NM, Neil CW, Purswani P, Li W, Meng M, Iyare U, Gross MR. Laboratory study of cyclic underground hydrogen storage in porous media with evidence of a dry near-well zone and evaporation induced salt precipitation. Int J Hydrogen Energy 2024;71:515–27. https://doi.org/10.1016/j.ijhydene.2024.05.234. 2024.
[43] Wiegand G, Franck EU. Interfacial tension between water and non-polar fluids up to 473 K and 2800 bar. Ber Bunsen Ges Phys Chem 1994;98(6):809–17. https://doi.org/10.1002/bbpc.19940980608.
[44] NIST. The chemistry webbook [online], https://www.nist.gov/programs-projects/nist-chemistry-webbook; 2023.
[45] Rushton JC, Hannis S, Pearce J, Williams J, Milodowski AE. Diagenetic evolution of the Bunter Sandstone Formation and its controls on reservoir quality: implications for CO_2 injectivity and storage. Geoenergy 2025;3(Issue 1). https://doi.org/10.1144/geoenergy2024-023. 2025.
[46] Yekta AE, Manceau J-C, Gaboreau S, Pichavant M, Audigane P. Determination of hydrogen–water relative permeability and capillary pressure in sandstone: application to underground hydrogen injection in sedimentary formations. Transp Porous Med 2018;122:333–56. https://doi.org/10.1007/s11242-018-1004-7. 2018.
[47] Jangda Z, Menke H, Busch A, Geiger S, Bultreys T, Lewis H, Singh K. Pore-Scale visualization of hydrogen storage in a sandstone at subsurface pressure and temperature conditions: trapping, dissolution and wettability. J Colloid Interface Sci 2023;629(Part B):316–25. https://doi.org/10.1016/j.jcis.2022.09.082. January 2023.
[48] Valvatne PH, Blunt MJ. Predictive pore-scale modeling of two-phase flow in mixed wet media. Water Resour Res 2004;40:W07406. https://doi.org/10.1029/2003WR002627.
[49] Imperial College. *Pore Occupancy Analysis* [computer programme]. https://github.com/ImperialCollegeLondon/poreOccupancyAnalysis; 2024.
[50] Raeini AQ, Bijeljic B, Blunt MJ. Generalized network modeling: network extraction as a coarse-scale discretization of the void space of porous media. Phys Rev E 2017;96(1):013312. https://doi.org/10.1103/PhysRevE.96.013312. 2017.
[51] Heap MJ. The influence of sample geometry on the permeability of a porous sandstone. Geosci Instrum Method Data Syst 2019;8:55–61. https://doi.org/10.5194/gi-8-55-2019.
[52] Hydrogen Analysis Resource Center. Hydrogen Viscosity at different temperatures and pressures [Online], https://h2tools.org/hyarc; 2024.
[53] Chow YTF, Maitland GC, Trusler JPM. Interfacial tensions of (H2O + H2) and (H2O + CO2 + H2) systems at temperatures of (298–448) K and pressures up to 45 MPa. Fluid Phase Equilib 2018;475:37–44. https://doi.org/10.1016/j.fluid.2018.07.022.
[54] Buades A, Coll B, Morel JM. Nonlocal image and movie denoising. Int J Comput Vision 2008;76:123–39. https://doi.org/10.1007/s11263-007-0052-1. 2008.
[55] Jennings JB. Capillary pressure techniques: application to exploration and development geology. AAPG 1987;71:1196–209.
[56] Lysyy M, Føyen T, Johannesen EB, Fernø M, Ersland G. Hydrogen relative permeability hysteresis in underground storage. Geophys Res Lett 2022;49. https://doi.org/10.1029/2022GL100364.
[57] Higgs S, Wang YD, Sun C, Ennis-King J, Jackson SJ, Armstrong RT, Mostaghimi P. Direct measurement of hydrogen relative permeability hysteresis for underground hydrogen storage. Int J Hydrogen Energy 2024;50:524–41. https://doi.org/10.1016/j.ijhydene.2023.07.270.
[58] Chabab S, Kerkache H, Bouchkira I, Poulain M, Baudouin O, Moine E, Ducousso M, Hoang H, Galliéro G, Cézac P. Solubility of H2 in water and NaCl brine under subsurface storage conditions: measurements and thermodynamic modelling. Int J Hydrogen Energy 2023;50:648–58. https://doi.org/10.1016/j.ijhydene.2023.10.290. 2024.
[59] Boon M, Rademaker T, Widyananda Winardhi C, Hajibeygi H. Multiscale experimental study of H_2/brine multiphase flow in porous rock characterizing relative permeability hysteresis, hydrogen dissolution, and Ostwald ripening. Sci Rep 2024;14:30170. https://doi.org/10.1038/s41598-024-81720-4.
[60] Al-Yaseri A, Fatah A, Al-Abdrabalnabi R, Alafnan S, Salmachi A. Investigation of gas residuals in sandstone formations via X-ray core-flooding experiments: implication for subsurface hydrogen storage. Int J Hydrogen Energy 2024;78:268–78. https://doi.org/10.1016/j.ijhydene.2024.06.244.
[61] Chiquet P, Daridon J-L, Broseta D, Thibeau S. *CO2/water interfacial tensi*ons under p*ressure and temperature conditions of CO2 geological storage*. Energy Convers Manag 2007;48:736–44. https://doi.org/10.1016/j.enconman.2006.09.011.
[62] Rotevatn A, Sandve TH, Keilegavlen E, Kolyukhin D, Fossen H. Deformation bands and their impact on fluid flow in sandstone reservoirs: the role of natural thickness variations. Geofluids 2013;13:359–71. https://doi.org/10.1111/gfl.12030. 2013.
[63] Singh K, Menke H, Andrew M, Lin Q, Rau C, Blunt MJ, Bijeljic B. Dynamics of snap-off and pore-filling events during two-phase fluid flow in permeable media. Sci Rep 2017;7:5192. https://doi.org/10.1038/s41598-017-05204-4. 2017.
[64] Heggernes H, Rotevatn A, Demurtas M, Nixon CW, Fossen H. Spatial variability in topology, connectivity and permeability of deformation band networks: insights from the Jurassic Entrada Sandstone, Utah. J Struct Geol 2023;176:104951. https://doi.org/10.1016/j.jsg.2023.104951.
[65] Romano CR, Garing C, Minto JM, Benson SM, Shipton ZK, Lunn RJ. Extreme capillary heterogeneities and *in situ* fluid compartmentalization due to clusters of deformation bands in sandstones. Int J Greenh Gas Control 2021;106:103280. https://doi.org/10.1016/j.ijggc.2021.103280. 2021.
[66] Lysyy M, Liu N, Solstad CM, Fernø MA, Ersland G. Microfluidic hydrogen storage capacity and residual trapping during cyclic injections: implications for underground storage. Int J Hydrogen Energy 2023;48:31294–304. https://doi.org/10.1016/j.ijhydene.2023.04.253.
[67] Zhang Y, Bijeljic B, Gao Y, Goodarzi S, Foroughi S, Blunt MJ. Pore-Scale observations of hydrogen trapping and migration in porous rock: demonstrating the effect of ostwald ripening. Geophys Res Lett 2023;50. https://doi.org/10.1029/2022GL102383.
[68] Dokhon W, AlZaabi A, Bijeljic B, Blunt MJ. Pressure decline and gas expansion in underground hydrogen storage: a pore-scale percolation study. Int J Hydrogen Energy 2024;86:261–74. https://doi.org/10.1016/j.ijhydene.2024.08.139.
[69] Dokhon W, Alzaabi A, Bijeljic B, Blunt M. Micro-Ct imaging of drainage and spontaneous imbibition for underground hydrogen storage in saline aquifers [online], https://doi.org/10.2139/ssrn.5117152; 2025.
[70] Goodarzi S, Zhang G, Bijeljic B, Blunt MJ. Ostwald ripening leads to less hysteresis during hydrogen injection and withdrawal: a pore-scale imaging study. Int J Hydrogen Energy 2025;114:475–85. https://doi.org/10.1016/j.ijhydene.2025.02.066. 2025.
[71] Guo R, Ershadnia R, Wang H, Hosseini SA, Zhao Q. Microfluidic experiments on hydrogen behavior in heterogeneous rocks during underground hydrogen storage in saline aquifers. Fuel 2025;391:134731. https://doi.org/10.1016/j.fuel.2025.134731. 2025.
[72] Bagheri M, Mahani H, Ayatollahi S, Zivar D. Direct pore-scale simulation of the effect of capillary number and gas compressibility on cyclic underground hydrogen storage & production in heterogeneous aquifers. Adv Water Resour 2023;181:104547. https://doi.org/10.1016/j.advwatres.2023.104547.
[73] Bi Z, Guo Y, Yang C, Wang L, He Y, Guo W. Numerical investigation of fluid dynamics in aquifers for seasonal large-scale hydrogen storage using compositional simulations. Renew Energy 2025;239:122101. https://doi.org/10.1016/j.renene.2024.122101.
[74] Mirchi V, Dejam M, Alvarado V. Interfacial tension and contact angle measurements for hydrogen-methane mixtures/brine/oil-wet rocks at reservoir conditions. Int J Hydrogen Energy 2022;47:34963–75. https://doi.org/10.1016/j.ijhydene.2022.08.056.
[75] Muhammed NS, Haq B, Al Shehri DA. Hydrogen storage in depleted gas reservoirs using nitrogen cushion gas: a contact angle and surface tension study. Int J Hydrogen Energy 2023;48:38782–807. https://doi.org/10.1016/j.ijhydene.2023.06.208.
[76] Malki ML, Chellal H, Mao S, Rasouli V, Mehana M. A critical review of underground hydrogen storage: from fundamentals to applications, unveiling future frontiers in energy storage. Int J Hydrogen Energy 2024;79:1365–94. https://doi.org/10.1016/j.ijhydene.2024.07.076.